Remote Sensing of Environment 202 (2017) 199–209

Contents lists available at ScienceDirect

Remote Sensing of Environment

journal homepage: www.elsevier.com/locate/rse

Consolidation settlement of Salt Lake County tailings impoundment revealed by time-series InSAR observations from multiple radar satellites

Xie Hu [a], Thomas Oommen [b], Zhong Lu [a,*], Teng Wang [a], Jin-Woo Kim [a]

[a] Roy M. Huffington Department of Earth Sciences, Southern Methodist University, Dallas, TX 75275, United States
[b] Department of Geological and Mining Engineering and Sciences, Michigan Technological University, Houghton, MI 49931, United States

ARTICLE INFO

Article history:
Received 16 July 2016
Received in revised form 30 March 2017
Accepted 19 May 2017
Available online 1 June 2017

Keywords:
Multi-temporal and multi-spaceborne SAR datasets
Time-series InSAR analysis
Tailings impoundment
Consolidation settlement
Stability monitoring

ABSTRACT

Tailings impoundment failures may lead to catastrophically fatal, environmental and financial consequences. Monitoring the stability of tailings facility is therefore indispensable for sustainable mining development. Particularly, tailings experience gradual consolidation settlement as the pore pressure dissipates and the terrain subsides. However, field investigations and geotechnical analysis at tailings impoundment are limited by sparse field instrumentation due to high cost. Interferometric Synthetic Aperture Radar (InSAR) can provide a full spatial view of settlement rate at millimeter-scale precision with bi-weekly or monthly updates. Here we integrate big remotely sensed data including multi-temporal and multi-spaceborne SAR images of ENVISAT, ALOS PALSAR-1, and Sentinel-1A, and SRTM DEM and LIDAR DEM, as well as water level data, to investigate the dynamics of consolidation settlement over the tailings impoundment area in the vicinity of Great Salt Lake, Utah. We show that the reclaimed south pond is experiencing enormous quasi-linear settlements with the largest rate of 200 + mm/yr around the low-permeable decant pond clay at the northeast corner during 2004–2011, and the rate decreases to 100 + mm/yr during 2015–2016. The nearly decadal InSAR measurements can be well-explained by geotechnical consolidation model, which reveals the long-term exponentially decaying settlement and predicts the settlement process in the near future. InSAR-derived displacement maps also highlight active motions of surrounding infrastructures, such as some highway segments. There is no clear evidence that the fluctuating deformation at those locations and seasonal varied water level are correlated. Our results demonstrate that high-resolution surface displacement measurements from InSAR can significantly improve our understanding of tailings settlement process and facilitate the monitoring of dams/infrastructures stability.

1. Introduction

Tailings impoundments/dams are built to accommodate the byproducts of mining operations after the separation of the valuable metals/minerals and the fine-grained wastes (tailings), and they can be usually found at or near mine sites (Hudson-Edwards, 2016). Since the mining industry produces enormous quantities of fine rock particles, ranging from a few millimeters down to as small as a few microns, the tailings embankment can reach several hundred meters in height and the impoundments can cover several square kilometers spatially (U.S. EPA, 1994). The failures of tailings dams occur worldwide (e.g., Caldwell and Charlebois, 2010), and the substantial triggering factors include, but not limited to, earthquake, foundation/slope failure, liquefaction, and overloading. A catastrophic tailings dam failure can have significant fatal, environmental, and financial consequences (Hudson-Edwards, 2016). The recent huge collapse of mines and tailings dams in Hpakant, Kachin state, Myanmar on November 21, 2015 killed at least 113 people (WISE, 2015). The failure can also cause the contamination of the ground surface and groundwater by the metals, and a large one can cost an average of $500 million for cleanup (Bowker and Chambers, 2015). The safety of the tailings facilities, for protecting life, environment, and property, is crucial in today's mining operations (ICOLD, 2001). Therefore, monitoring the stability of tailings impoundment is critical for sustainable mining development. However, the overwhelming spatial extent of the tailings impoundment often proves to be an engineering challenge to monitor using traditional geotechnical measurement techniques.

Interferometric Synthetic Aperture Radar (InSAR) provides an excellent monitoring tool to evaluate the stability of man-made structures, such as the newly employed field of tailings dams (e.g., Riedmann et al., 2013; Colombo, 2013; Necsoiu and Walter, 2015), by providing mm-scale precision deformation measurements with bi-weekly or monthly updates. The rate of settlement and its spatial distribution derived by InSAR can help determine if the desired consolidation is reached, if additional drainage needs to be performed, and where the

* Corresponding author.
E-mail address: zhonglu@smu.edu (Z. Lu).

http://dx.doi.org/10.1016/j.rse.2017.05.023
0034-4257/

drainage wells should be installed. It also can provide indications of any differential settlement occurring within the impoundment. However, those recent InSAR studies on tailings impoundment in South Africa (Riedmann et al., 2013), Chile (Colombo, 2013), and New Mexico (USA) (Necsoiu and Walter, 2015) were mainly focused on the dams' slope stability, but their geotechnical mechanism, potential impacts to the surrounding area, and correlation with the hydrological processes have been less investigated (Riedmann et al., 2013; Colombo, 2013). Besides, the analysis was limited by the availability of archived SAR images (e.g., short temporal period) and also was in lack of validation (Necsoiu and Walter, 2015). Our study presented here is the first that uses a combination of multi-temporal and multi-spaceborne SAR observations, digital elevation models (DEMs) from SRTM and high-resolution LIDAR, and auxiliary water level data, to assess the stability of Kennecott tailings impoundment in Salt Lake County, Utah, and the surrounding area. A set of 40 descending C-band ENVISAT ASAR images from Track 41 (T41) during 2004–2010, 13 ascending L-band ALOS PALSAR-1 fine beam mode images from Path 202 (P202) during 2007–2011, and 18 ascending C-band Sentinel-1A interferometric wide-swath (IW) images from Path 158 (P158, half of the imaging swath) during 2015–2016 were used in our study (Fig. 1A). Utilizing a large dataset of SAR images can a) improve the accuracy of deformation measurement through multi-interferogram processing by reducing various artifacts in individual interferograms, b) enhance the temporal resolution of the time-series products, c) allow for the retrieval of 2-dimensional (or even 3-dimensional) deformation vectors, and d) expand the time span of the investigation to better understand the long-term characteristics of the phenomenon (e.g., Lu and Dzurisin, 2014). Our multi-temporal InSAR method assesses the stability of the embankments through mapping out the drastic and gradually decelerated subsidence over the south pond, and various deformation behavior over the surrounding infrastructures and land disposal sites. We also compare InSAR-derived deformation with daily water level data. We show that InSAR observations can be well-explained by our consolidation settlement model, which allows us to differentiate the settlement process and foresee its development in the near future.

2. Study area and related hazards

The east flank of Oquirrh Mountains at Salt Lake Valley, Utah, accommodates the Bingham Canyon mine managed by Kennecott Utah Copper Company that contributes to a quarter of the copper in US. Tertiary-age igneous rocks intruded the Oquirrh Formation, forming deposits of copper and other metals that have been extracted with a depth of >970 m (Pankow et al., 2014). Around 20 km north to the Bingham Canyon mine, Kennecott built a 37-km^2 tailings impoundment to contain its uneconomic ore products, which has been in operation since 1906. Tailings in the impoundment are primarily composed of silica sand, with a slightly higher concentration of copper than the general soil in the western United States (Kennecott Utah Copper, 2008).

Kennecott tailings impoundment, together with a mining refinery and a smelter, are in close proximity to the Great Salt Lake (Fig. 1B). The tailings show a downward hydraulic gradient, equal to an average of 40% hydrostatic pressure (Klohn Leonoff, 1992). The aquifer systems around the impoundment have concentrations of arsenic, selenium, and cadmium in excess of Utah Ground Water Quality Standards (Kennecott Utah Copper, 2011). Currently, there is an increasing public awareness about the extensive groundwater contamination and air pollution from mining production, and their impact to the fish and wildlife habitats in the Great Salt Lake and the residential community Magna (EARTHWORKS, 2011).

Another big concern is the stability of the facility and the associated risk to public safety due to a potential earthquake induced failure (URS, 1999a; URS, 1999b; Tetra Tech, Inc., 2009). Kennecott tailings impoundment has experienced failures in 1941, 1964 and 1998 (Kennecott Utah Copper, 1997; AGRA Earth, and Environmental, Inc., 1998). The deposition of fine particle tailings became fluid due to water intrusion, resulting in embankment failure. The impoundment is located between

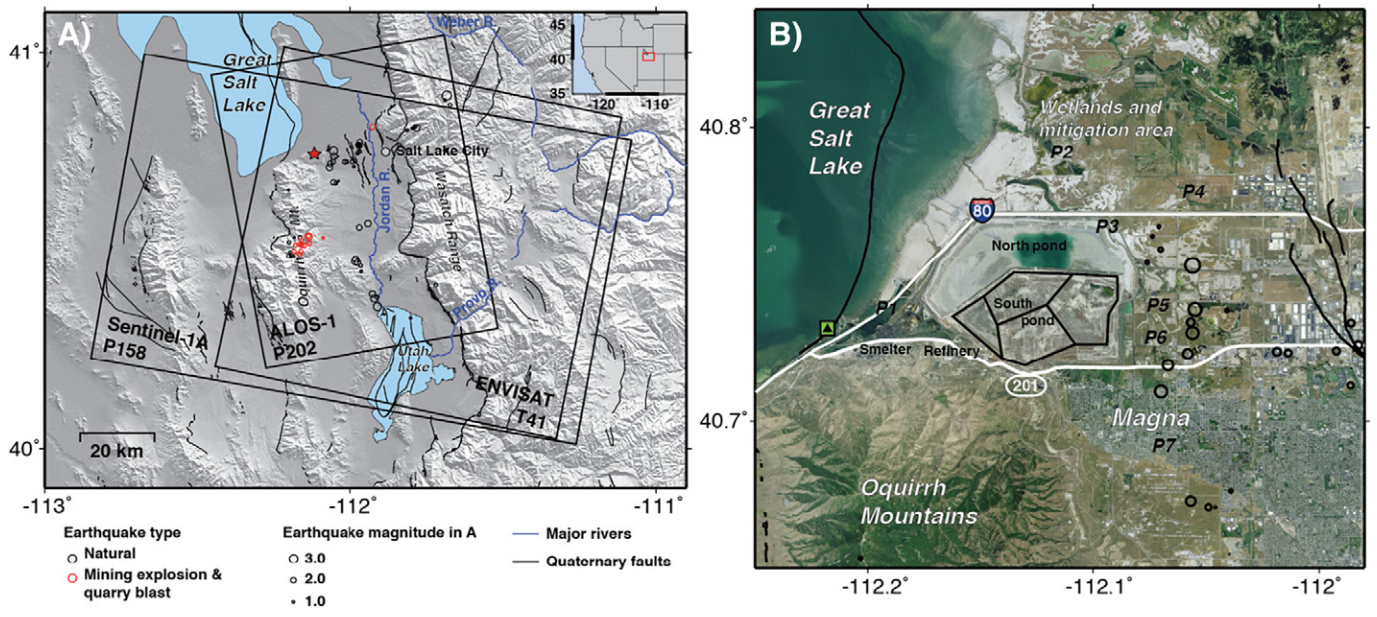

Fig. 1. (A) Coverage of radar data tracks (black squares) superimposed on the shaded relief map over Salt Lake Valley, Utah. Black lines show the Quaternary faults and blue lines represent major rivers and streams. Circles indicate locations of earthquakes occurred in recent decade, in which black ones are tectonic earthquakes and red ones (concentrated at the Bingham Canyon mine) are caused by mining explosion and/or quarry blast. Earthquake magnitudes are proportional to the size of the circles. Tailings impoundment, denoted with the star, locates in the vicinity of the Great Salt Lake. (B) Aerial imagery of the tailings impoundment bounded by the Great Salt Lake to the northwest, wetlands and mitigation area to the northeast, Oquirrh Mountains to the southwest, and residential community Magna to the southeast. The whole impoundment can be classified into two major ponds – the north pond with active tailings deposition and the south pond which has been completely abandoned and reclaimed since 2001. The south pond can be further divided into four reclamation areas by the ditches (visible from the aerial images and LIDAR DEM shade relief map), and they are outlined by black polygons. Interstate Hwy I-80 and state Hwy 201 are delineated with white lines. The water gage at Saltair Boat Harbor is marked with the triangle inside the green square near the intersection of Hwys I-80 and 201. Same symbols are used in the other figures in this paper.

the East Great Salt Lake fault zone to the west and the extended fault segments of the Wasatch fault system to the east (EERI, 2015). Fig. 1B illustrates the tectonic earthquakes in this valley mainly occurred at the terrain adjacent to tailings dams, suggesting the fluid pressure change may vary the stress field and trigger the seismicity, which in turn, may induce liquefaction and the associated dam failure and runout event.

To upgrade the stabilization of the old south pond in the vicinity of Magna community, Kennecott began reducing the slope of the southeast corner and moved the tailings >800 m away from the slope crest in the early 1990s (Kennecott Utah Copper, 2008). In 1995, Kennecott added an adjacent 14-km^2 north pond with seismic upgrade, and later in 1999, began transitioning from the south pond to the north pond (Kennecott Utah Copper, 2008) (Fig. 1). Kennecott actively managed the suppression of dust at the north pond by keeping the center (where fine grain tailings are deposited) wet with tailings slurry and watering the outer embankments (UDEQ and EPA, 2014). After terminating the tailings deposition on the south pond completely in 2001, Kennecott reclaimed the area by vegetating the slopes and top surface, which included a series of implementations of dewatering (UDEQ and EPA, 2014). Around the perimeter of the impoundment, clarification canal and toe drains have been constructed to collect the water. A sedimentation pond (P5 in Fig. 1B) to the east side of the south pond was used for further clarification of the drain-down water to reduce total suspended solids before directing the water to the process circuit (Kennecott Utah Copper, 2011). Kennecott has spent over $500 million dollars in the past 20 years to consistently upgrade the stability of the south tailings facility, and recently launched another $2 million pilot dewatering project to accelerate the stabilization process, which included the installation of more wells for water pumping (Kennecott Utah Copper, 2016).

Even though enormous efforts have been put forth to mitigate the risk of failure (Kennecott Utah Copper, 1997; EARTHWORKS, 2011), there is no geodetic measurements to systematically monitor the settlement of tailings and the stability of the surrounding area. Persistent consolidation settlement due to the dissipation of pore pressure and the associated increase in effective stress during water drainage and extraction may pose a threat to the surrounding infrastructures, including a major railway line, Interstate Hwy I-80 and State Hwy 201 (Fig. 1). It is especially indispensable to monitor the stability of the impoundment area in this tectonically active region. Utah Department of Environmental Quality (UDEQ) and Environmental Protection Agency (EPA) claimed that the south pond, the outer embankments of the north pond, and the surface soils along the south side of Hwy 201 appeared to be stable in their recent five-year review [2014]. However, the statement needs to be thoroughly investigated by long-term precise observations.

3. Multi-temporal InSAR analysis

We employ a multi-temporal InSAR data processing routine to derive the displacement field after removing the atmospheric phase screen and orbital artifacts inherent in each interferogram (e.g., Hu et al., 2016). The topographic phase component in the interferograms is estimated using 2-m resolution bare-earth LIDAR DEM acquired in 2006. A total number of 105 ENVISAT ASAR interferograms (perpendicular baseline < ~300 m and temporal interval < ~450 days), 23 ALOS PALSAR-1 interferograms (perpendicular baseline < ~2000 m and temporal interval < ~600 days), and 66 Sentinel-1A interferograms (perpendicular baseline < ~250 m and temporal interval < ~180 days) are used for time-series analysis. Fig. 2A–C show the baseline configurations for these three datasets, respectively.

We jointly use the dispersion of amplitude (DA) and averaged coherence to identify persistent scatterer (PS) (Ferretti et al., 2000). The north pond completely loses coherence due to moist surface for the purpose of enhanced dust control, and thus no PS point can be detected. The south pond has been reclaimed and well-vegetated at the surface that allows for the identification of PS points. Although the south pond is claimed no longer active in tailings deposition, it is still valuable to evaluate Kennecott's commitment of reclamation and stabilization efforts to sustainable development, especially when the tailings still have the potential to liquefy at this tectonically active region. The available ENVISAT and Sentinel-1A images are sufficiently large in number, and thus we exclude the data acquired during winter season from December to February when the coherence is poor. Nevertheless, the available ALOS-1 images are limited, so we include all data running through different seasons. The south pond has been kept wet for the purpose of dust control, which makes the top layer frozen in winter so that SAR amplitude is highly varied in time. Therefore, the DA of ALOS-1 over the south pond is significantly larger than that of the other two datasets, and its detected PS points at the south pond are much sparser than the surrounding area at given DA threshold. The disparity in density is less obvious for ENVISAT dataset and almost ignorable for Sentinel-1A dataset. To achieve a general density equilibrium of PS points between the south pond and the surrounding areas for ENVISAT and ALOS-1 datasets, we first apply ordinary thresholds (DA < 0.5 and averaged coherence > 0.35 for ENVISAT dataset, and DA < 0.4 and averaged coherence > 0.5 for ALOS-1 dataset) to obtain the initial PS points in the study area (Fig. S1A and D), and then loosen the thresholds (DA < 1 and averaged coherence > 0.32 for ENVISAT dataset, and DA < 1 and averaged coherence > 0.4 for ALOS-1 dataset) to densify PS points within the south pond (Fig. S1B and E). A merge of those two constitutes the ultimate PS points (Fig. S1C and F) used for time-series analysis. Sentinel-1A images are regularly acquired over this study site with around 24-day intervals (the satellite repeat cycle is 12 days), leading to much larger

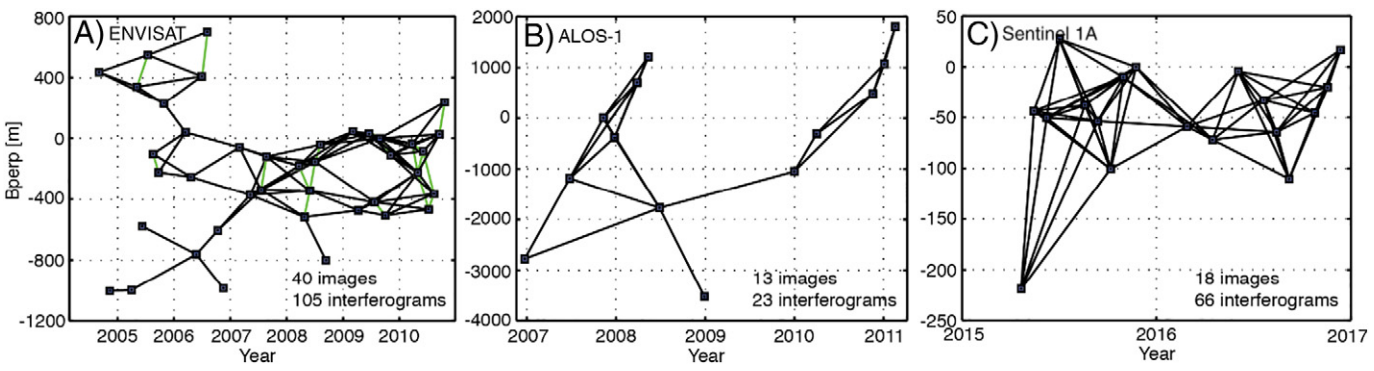

Fig. 2. Baseline configuration of ENVISAT (A), ALOS-1 (B) and Sentinel-1A (C) datasets. All connecting lines indicate the interferograms used to retrieve the time-series deformation, in which the green lines in plate A represent the interferograms used to estimate the dominant deforming trend at the south pond.

coherence and smaller DA, and we use the same thresholds (DA < 0.45 and averaged coherence > 0.5) for the entire study area. The resultant averaged density is 1200, 1600 and 1350 PS points per km^2 for ENVISAT, ALOS-1 and Sentinel-1A datasets, respectively.

As our study area is adjacent to the Great Salt Lake at the foot of Oquirrh Mountains, water vapors accumulated above the air can produce artifacts in interferograms. Considered as low frequency signal in space, atmospheric artifacts and satellite orbital errors are estimated by first-order polynomial fitting with respect to the range and azimuth position in radar coordinates as well as the elevation at the location of PS points. The actively moving south pond and poorly coherent mountainous areas are masked out when constraining the polynomial coefficients.

The deformation gradient in the tailings impoundment based on initial interferograms is too large for C-band ENVISAT dataset to be correctly unwrapped. To resolve the heavily condensed fringes in terms of interferograms, we first estimate the linear deformation velocity using 19 interferograms with stringent baseline thresholds (perpendicular baseline < ~300 m and temporal interval < ~90 days, green connecting lines in Fig. 2A). The velocities for each PS points are further used to estimate the dominant deformation component, which is removed from the original wrapped phase for all the selected 105 interferogram. As a result, the fringes of the interferograms are greatly reduced that allows for correct phase unwrapping. Thereafter, the dominant deformation component is added back. This process can be run iteratively, and the dominant deformation component is re-estimated from each iteration. In our study, two iterations are good enough to eliminate the phase jumps. The resultant 105 unwrapped interferograms are used to retrieve the time-series deformation at each PS point using least-squares estimation (e.g., Hu et al., 2016). Although Sentinel-1A dataset is also operated at C-band, the temporal frequency (~9 acquisitions per year used in this study) is much improved than ENVISAT (~6 acquisitions per year), so we can have sufficient number of interferograms with clearly distinguishable fringes to avoid unwrapping problem.

4. Data analysis and interpretation

Assuming that there is no north-south movement on the south pond, we can derive the 2-D (vertical and east-west) displacement field (Fig. 3) using the temporally overlapping measurements of ENVISAT and ALOS-1. The ground surface shows significant land subsidence, reaching a rate of 200 + mm/yr at the northeast corner; which is a representation of the vertical settlement of the tailings impoundment during dewatering. Interestingly, the horizontal displacement map shows the west and east parts of the south pond move toward the center, though at a much smaller magnitude (<30 mm/yr). This might be duo to the possible surface motion of the south pond toward the central north pond (greenish surface area in Fig. 1B) that is currently in active tailings deposition. Considering the tailings fields are governed by the vertical motion, we retrieve the vertical deformation by projecting the radar line-of-sight (LOS) deformation with the local incidence angle at each PS point in the following analysis.

4.1. Drastic settlement of the south pond

The vertical deformation velocity of the study area (Fig. 4A–C) and the deformation velocity measurements along two profiles AA′ and BB′ (Fig. 4D–E, for PS points within a buffer of 100 m) suggest that the settlement has been gradually decelerated throughout the entire south pond. Three independent InSAR datasets show good consistency that the compaction peak locates at the northeast corner at a rate of 200 + mm/yr during 2004–2011 and 100 + mm/yr during 2015–2016; the adjacent toe of the north slope just west of the northeast corner is where the statically-induced flow liquefaction slide occurred in 1998 (AGRA Earth, and Environmental, Inc., 1998). The settlement seems to be well constrained by the peripheral embankments. Although the time span of Sentinel-1A imagery is only around two years, the temporal resolution is high enough to maintain good coherence, so the averaged velocity map can pinpoint the location of the compaction peak, where ENVISAT and ALOS-1 datasets failed due to the scarcity of PS points. In addition to drastic subsidence, the entrapped water over the fine-grained tailings is another explanation for the scarcity of PS points at this location. The water used in the slurry transport of tailings on the south pond has been collected in a decant pond in the near vicinity of the northeast corner since 1917 (Dunne et al., 1999).

The 2006 LIDAR DEM, 2000 SRTM DEM and their difference over the study area are shown in Fig. S2 A–C. According to the DEM map, the impoundment areas are significantly higher (approximately 65 m) than the surrounding ground, consistent with the investigation conducted by the UDEQ and EPA (2014). Additionally, the embankments confining

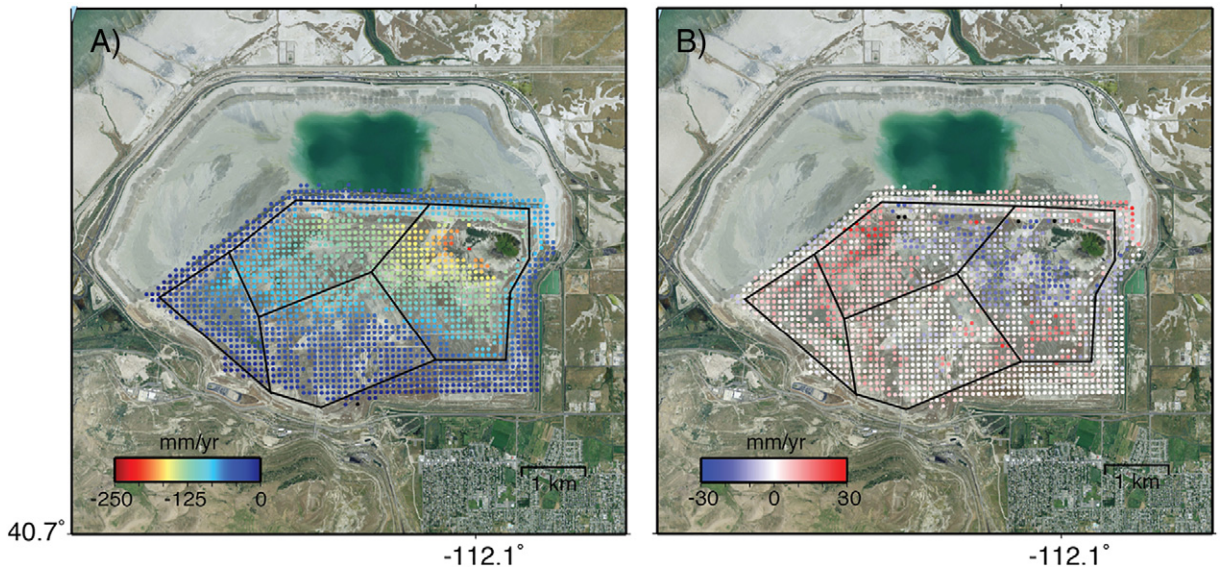

Fig. 3. 2-D annual displacement (assuming no north-south movement) field of the south pond derived by ENVISAT and ALOS-1 measurements of overlapping period between 2007 and 2010. (A) Vertical displacement field. Negative values mean subsidence. (B) Horizontal east-west displacement field. Positive values mean eastward motion and negative values mean westward motion.

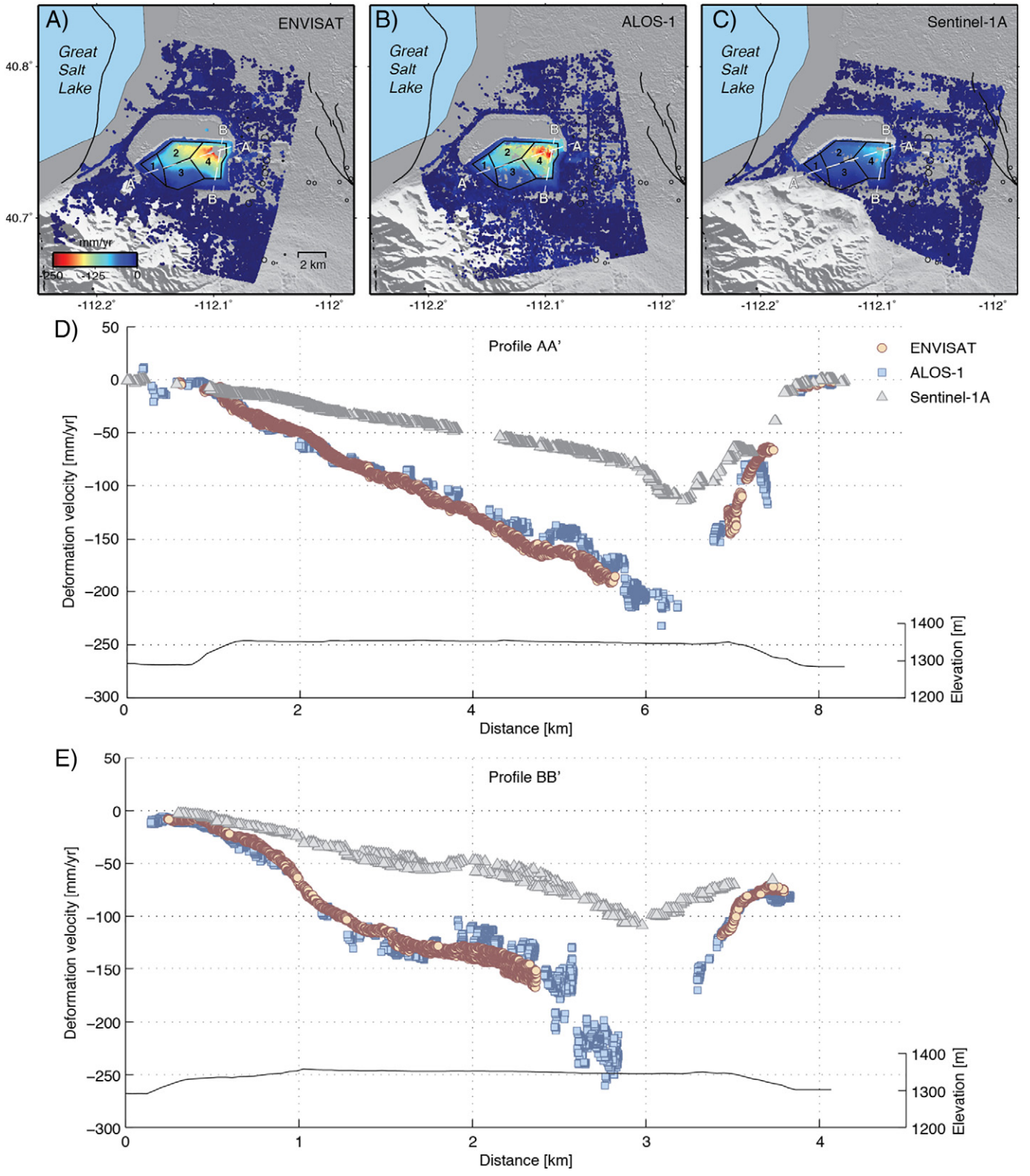

Fig. 4. Vertical deformation velocity in the south pond derived from ENVISAT (A), ALOS-1 (B) and Sentinel-1A (C) datasets. D and E show the deformation velocities of ENVISAT (red circles), ALOS-1 (blue squares), and Sentinel-1A (gray triangles) along cross-section profiles AA′ and BB′ (white dashed lines). The left Y axis represents the vertical deformation velocity in millimeters per year and the right Y axis represents the elevation in meters.

the pond along the interstate Hwy I-80, and the tapered earthen berms next to the Magna neighborhood are also visible from the DEM difference map, suggesting they were built between 2000 and 2006: a linear structure with around 20-m increase of height along I-80 highlights the upgrade and construction of the embankments during this time period, and the linear features with >10-m decrease of height at the southeast

corner probably correspond to the ditches bounded the tapered earthen berms (approximately 4.5 m in height) (Kennecott Utah Copper, 2008). More importantly, the DEM difference map provides another evidence of the emplacement of the compaction peak (Fig. S2 D and E). InSAR and DEM estimations are in good agreement that the compaction peak locates at 6.5 km along profile AA′ (from A) and 3.05 km along profile BB' (from B).

The south pond was subdivided into some reclamation areas, and these areas were reclaimed in a systematic and sequential manner, while tailings continue to be deposited into the unreclaimed areas (URS, 1999a). A series of reclamation dikes constructed across the surface of the impoundment isolate each of the reclamation areas and allow us to delineate the major reclamation areas (polygons outlined by black lines in Figs. 1B, 3, 4A–C, and 6) according to the shaded relief map of LIDAR DEM and aerial imagery.

To better analyze the deformation patterns, we calculate the averaged cumulative deformation of each reclamation area. Fig. 5 shows that the least subsidence is observed at reclamation areas 1 and 3 to the west and south, and more than twice of the magnitude can be found at reclamation areas 2 and 4 to the north and east. The cumulative deformation from ALOS-1 results is slightly larger than that from ENVISAT, which is more outstanding in reclamation area 4. This is because the density of PS points over this most subsiding northeast corner is larger in ALOS-1 results than ENVISAT, so more significant values are included when taking the average. Another reason in favor for the difference between ENVISAT and ALOS-1 estimates might be due to the possible horizontal displacement, because descending track from ENVISAT and ascending track from ALOS-1 have different sensitivity to horizontal motions. Nevertheless, the difference in the cumulative deformation is small and can be ignored with respect to the total amount. Time-series deformation (Fig. 5) also suggests that the settlement has been decaying. Take the reclamation area 4 for example, Sentinel-1A results depict a cumulative averaged subsidence of almost 100 mm in less than two years from April 2015, indicative of a settling rate of ~50 mm/yr, around one quarter of that in previous years during 2004–2011 (an average of ~130 mm/yr as derived from ENVISAT and ALOS-1 results). We believe a couple of outliers in the time series are due to the localized atmospheric turbulence associated with the corresponding acquisitions.

4.2. Stability of the embankments and surrounding area

The settlement in the tailings impoundment and the accompanying drastic surface subsidence may have an impact on the stability of the embankments and surrounding area, underlain by the low permeability Upper Bonneville Clay. Based on multi-temporal InSAR results, we have found the northeast embankments of the south pond are in active motion (Fig. 6). Some long-term net subsiding sites can also be located: two segments along the Hwy I-80 (P1 and P3) and two wetlands and mitigation sites (P2 and P4), and the sedimentation pond (P5) and the land disposal site (P6). In contrast to the decaying settlement of the south pond, most of the highlighted sites seem to maintain the same level of deformation velocity through time. One segment of Hwy 201 adjacent to the embankments at the southeast corner experiences relatively subtle subsidence (~20 mm/yr), far less than that of the south pond, and the deformation boundary has retreated to keep further away from the residential community of Magna according to the recent Sentinel-1A results.

To better interpret the behavior of the occurring deformation, we plot the time-series deformation at selected sites, and also compare with the daily water level measurements at Saltair Boat Harbor in the vicinity of the Great Salt Lake (green square in Figs. 1B and 6). The sedimentation pond P5 (Fig. 7E) depicts quasi-linear subsidence, which is similar to the south pond (Fig. 5). Interestingly, the subsidence of P5 is at the same rate of decaying with respect to the settlement over the south pond. To be specific, the rate of subsidence of P5 has decreased from ~25 mm/yr during 2004–2011 to ~10 mm/yr during 2015–2016, similar to the decaying settling process (by around 60%) of the adjacent reclamation area 4 from ~130 mm/yr to ~50 mm/yr. Therefore, we may come to the conclusion that the subsidence of P5 is highly likely due to the settlement effect extended from the south pond. Around 3 km northeast to the impoundment, site P4 (Fig. 7D) seems to maintain a quasi-linear subsidence at a rate of 7 to 10 mm/yr. Site P7 (Fig. 7G) at Magna shows fluctuations of displacements, but the net elastic deformation is almost zero. The other selected sites, including the Hwy I-80 segments P1 (Fig. 7A) and P3 (Fig. 7C), wetlands and mitigation site P2 (Fig. 7B), and the land disposal site P6 (Fig. 7F), exhibit net cumulative subsidence up to 60 mm with large fluctuations from 2004 to 2011. The water level follows the seasonal trend, reaching the peak in the late spring and then dropping to the bottom in the early winter, with an annual peak-to-trough magnitude of <1 m. The time-series deformation of P6, particularly for Sentinel-1A results, seems to be in phase with water levels, possibly suggesting an elastic response of the ground surface to the pore pressure change; however, we can't find similar rhythm in other sites (e.g., P1–P5) closer to the water level gage. Nevertheless, we are still in lack of clear evidence on the correlation between deformation fluctuation and seasonal water level in this study site.

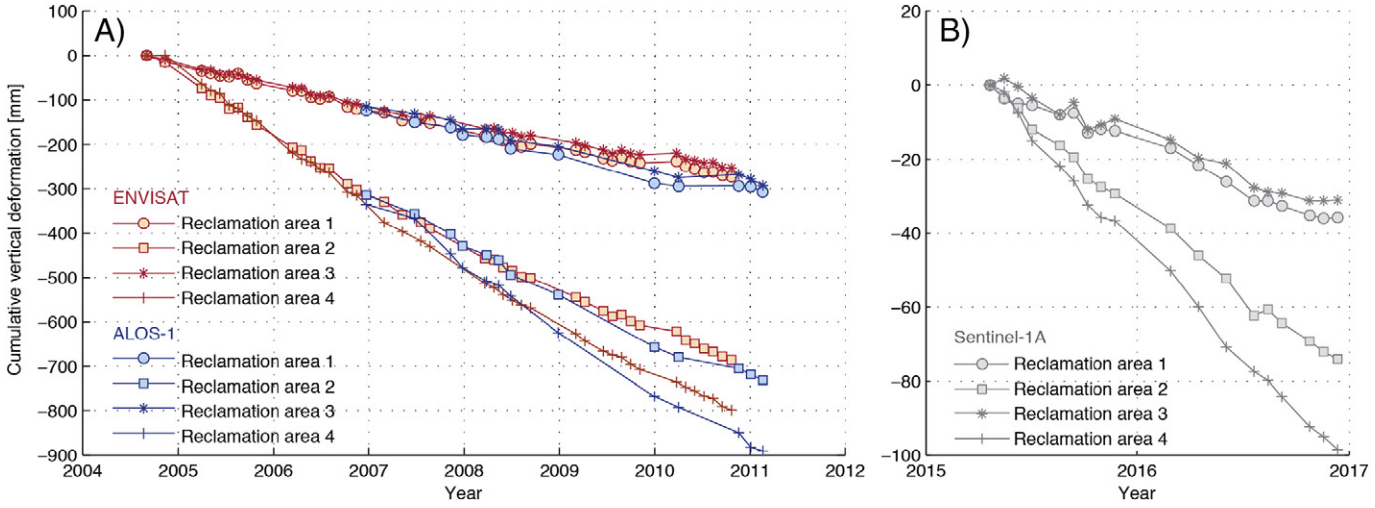

Fig. 5. Quasi-linear cumulative deformation of four reclamation areas within the south pond. Circles, squares, asterisks and crosses represent the results of reclamation areas 1 to 4, respectively. Red and blue annotations in plate A and gray annotations in plate B represent the measurements of ENVISAT, ALOS-1 and Sentinel-1A, respectively.

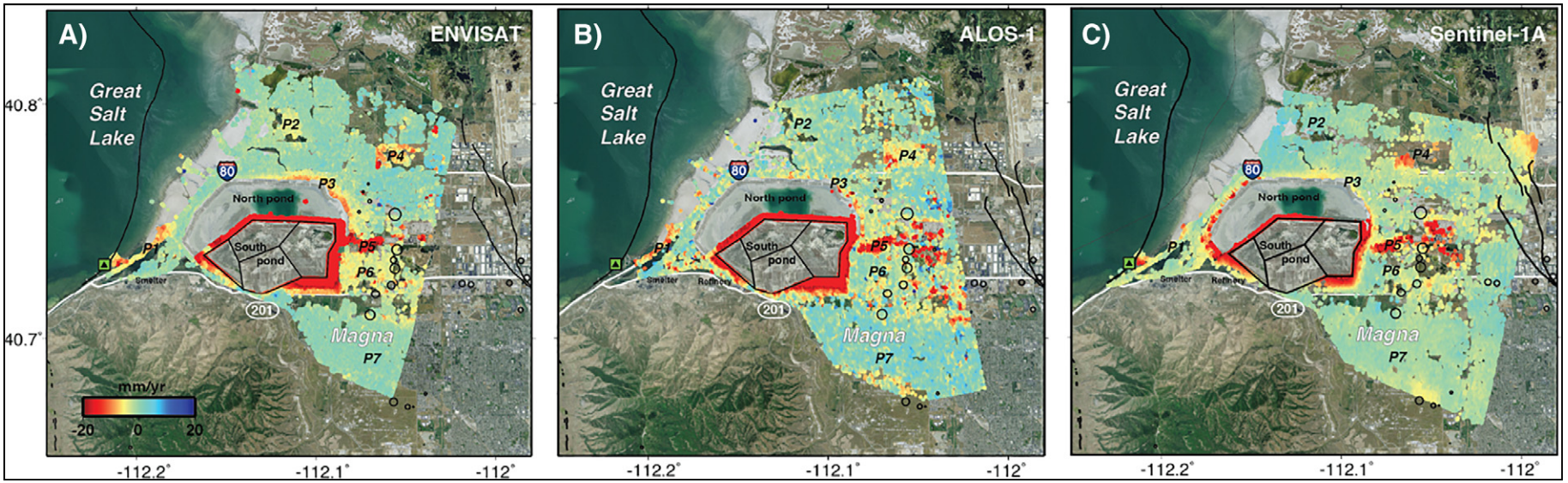

Fig. 6. Vertical deformation velocity surrounding the tailings impoundment derived from ENVISAT (A), ALOS-1 (B) and Sentinel-1A (C) datasets, respectively. The drastic settlement of south pond and the poorly coherent mountainous areas in the southwest of the study area are masked out so that we can highlight on our area of interest with a narrow range of colour scale.

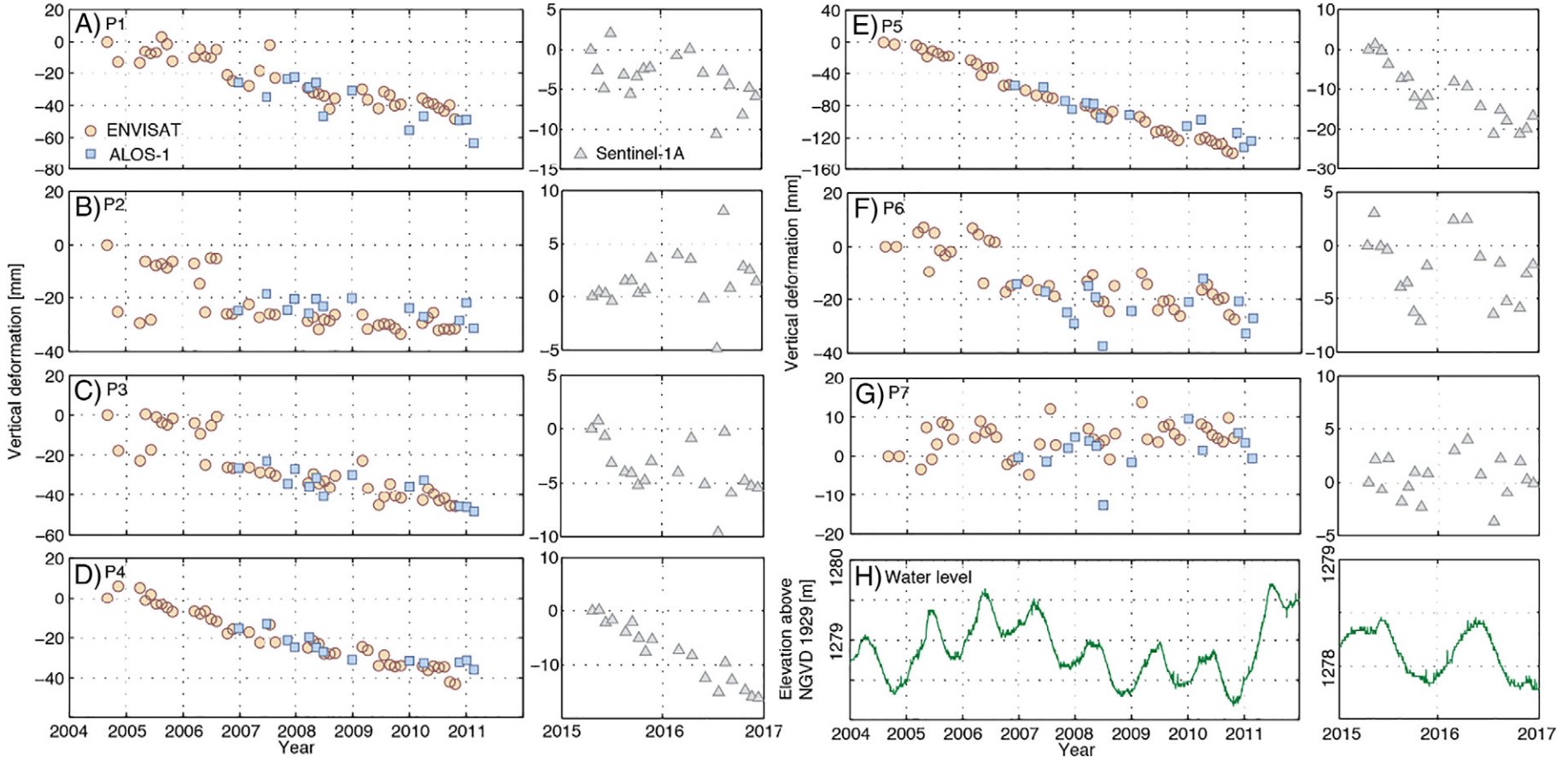

Fig. 7. Cumulative vertical deformation surrounding the impoundment and water level measurements. (A)–(G) Time-series vertical deformation of the selected sites P1–P7 whose locations are marked in Figs. 1B and 6. The measurements of ENVISAT, ALOS-1 and Sentinel-1A are denoted by the red circles, blue squares and gray triangles, respectively. (H) Daily water level measurements at Saltair Boat Harbor.

We believe that the embankments do constrain the drastic compaction of the impoundment to a fairly large extent, but there are still some "leakages" occurred. Based on our observations, we make the following recommendations: 1) stabilization of embankments along the east half side of the impoundment, 2) monitoring of the tailings-related process near the water gage at Saltair Boat Harbor and the sedimentation pond around P5, 3) reinforcement of the foundation of Hwy I-80 segments at the harbor around P1 and along the northern embankment around P3, as well as the Hwy 201 segment next to the southern part of the embankment, or a complete relocation of those highway segments, and 4) establishing buffering zones around the south and east slope near Magna.

5. Consolidation settlement modeling

The tailings field can be vertically stratified into five layers from top to bottom – spigotted tailings, soft tailings clay, deep whole tailings, Upper Bonneville clay and interbedded sediments (URS, 1999a). The surface is covered by the ~6-m thick spigotted tailings, similar to sandy beach deposits that belongs to whole tailings, and we consider it as the final load on the tailings structure. Immediately beneath the spigotted tailings layer is the ~10-m soft tailings clay, which is fine-grained and typically classifies as a low-to-medium plasticity silty clays, and the soft tailings clay around the northeast corner area is characterized as decant pond clay, which is in highly saturated condition and occupying the lowest elevation. The ~45-m layer of older deposits of deep whole tailings are highly interbedded and relatively coarse-grained in nature, and typically classified as a silty sand interbedded with silts and silty clays. The foundation of the tailings structure is composed of lake clays interbedded with lenses of sands. The Upper Bonneville clay is around 4 m and marked by Gilbert red beds, so called because of oxidation stains resulting in a reddish appearance. The tight clay strata are occasionally interrupted by sand beds, typically with <0.6-m thickness; generally, this layer effectively limits the seepage of process water into underlying foundation (Dunne et al., 1999). Interbedded sediments with various interbedded clays and sands sitting at the bottom have a thickness of ~15 m. The deposits of soft tailings clay and deep whole tailings have an over-consolidation ratio (OCR) of 1.5, attributed to aging and chemical alteration of tailings over time. Underneath the embankment, the maximum OCR of the foundation layers of the Upper Bonneville clay and interbedded sediments can reach 4.0 in the free field.

The settlement of overconsolidated tailings was analyzed using the software Rocscience Settle^{3D} (2009) based on the InSAR-derived surface displacement field. Soil material properties (Table 1) are selected adequately based on Kennecott's internal geotechnical reports (Dunne et al., 1999; URS, 1999a; URS, 1999b; Tetra Tech, Inc., 2009) and various documentations on soil properties (Carter and Bentley, 1991; Das, 2002; Das, 2008; Geotechdata info., 2013; Hough, 1969; McCarthy, 1998; Spangler and Handy, 1982; Swiss Standard, 1999).

Wick drains/prefabricated vertical drains could support a number of critical engineering requirements during the stability upgrade of the south pond and the construction of the expanded north tailings storage facility (Dunne et al., 1999). Wick drains were installed around the existing dewatering wells to enhance the drain flows by providing vertical drainage between various tailings layers. Two principal wick drain programs were implemented around the southeast and the northeast corners of the south pond. At the southeast corner, wick drains mainly focused on the eastern reach of the south slope, where hydraulic conductivity was relatively low, and consequently, the flow rates of tailings in this area were relatively slow. The installation followed a triangle pattern with a spacing of 4 m and an averaged depth of 33 m, and most of them were installed between December 1997 and July 1998 (URS, 1999b). At the northeast corner, the wick drain program was initiated after realizing significantly lower shear strength than anticipated over the slope at the northeast side of the south pond in 1992 (Dunne et al., 1999). The prompt field investigation suggested that the clay-sized soil materials in this area had not consolidated to a degree that can sustain the increasing overlying loads. The fine-grained nature of the tailings in this area had entrapped water and resulted in an increase of in situ pore pressures as new material deposition occurred. A series of wick drains were installed mainly at the embankment slope and beach area with a spacing of 2 m and an averaged depth of 60 m, which were believed among the deepest vertical drains installed in the world (Dunne et al., 1999), and the installation were completed between 1995 and 1998 (URS, 1999a).

Wick drain programs have been proven effective in controlling the excess pore pressure and enhancing the drainage characteristics within the upstream constructed tailings embankment (Dunne et al., 1999). Since horizontal permeability is usually higher than vertical permeability so that horizontal flow is faster, and we assume the ratio of horizontal to vertical permeability Kh/Kv is 2 for all the layers. Settlement analyses are carried out using an average pressure (111 kN/m^2) of the top spigotted tailings layer acting at remaining tailings structure starting from 2000 (the middle time between the installation of wick drains and the abandon of tailings deposition to the south pond). The surface settlement is assumed to be the imprint of the deformation at the interface of spigotted tailings and the underlying soft tailings clay at a depth of 6 m. In addition, to represent the groundwater condition, we added 0-m piezometric line at the layer of soft tailings clay, and 1-m piezometric line at the underlying layers. Wick drains at the southeast corner is along the periphery slopes; however, the coverage at the northeast corner is not accessible from literatures (Dunne et al., 1999; URS, 1999b), so we made assumptions based on InSAR-derived displacement field.

Total settlement is the sum of three components - immediate (elastic) settlement, primary consolidation, and secondary consolidation (creep) (Fig. 8A and C–E). Immediate settlement occurs instantly after loads are applied and is measured as >600 mm at the center of the loads in the model (Fig. 8C). Immediate settlement is assumed to be linear elastic, and it only depends on the total stress, not effective stress. Therefore, pore pressure changes due to settlement have no effect on the immediate settlement. When a load is applied to a low permeability material, a period of primary consolidation is normally expected after load is applied due to dissipating excess pore pressure. Afterwards, continuing settlement, which is known as secondary consolidation, may

Table 1
Soil material properties of tailings structure.

Soil layers	Thickness* [m]	Unit weight* [kN/m^3]	Immediate settlement	Primary consolidation					Secondary consolidation
			Es** [kPa]	Cc**	Cr**	e0**	OCR*	K*,** [mm/yr]	Cα**
Spigotted tailings (load)	6	18.54	14,000	0.36	0.050	0.8	1.2	3150	0.036
Soft tailings clay	10	16.81	2700	0.56	0.074	1.2	1.5	1	0.056
Deep whole tailings	45	18.22	14,000	0.41	0.056	0.8	1.2	100	0.041
Upper Bonneville clay	4	18.54	10,000	0.36	0.055	0.8	2.5	20	0.036
Interbedded sediments	15	20.26	32,500	0.26	0.039	0.8	2.5	100	0.026

Es: Young's modulus; Cc: compression index; Cr: recompression index; e0: initial void ratio; OCR: over-consolidation ratio; K: permeability; Cα: secondary compression ratio. Note: Soil material parameters are selected adequately based on Kennecott's internal geotechnical reports (superscript *) and other documentations on soil mechanism (superscript **).

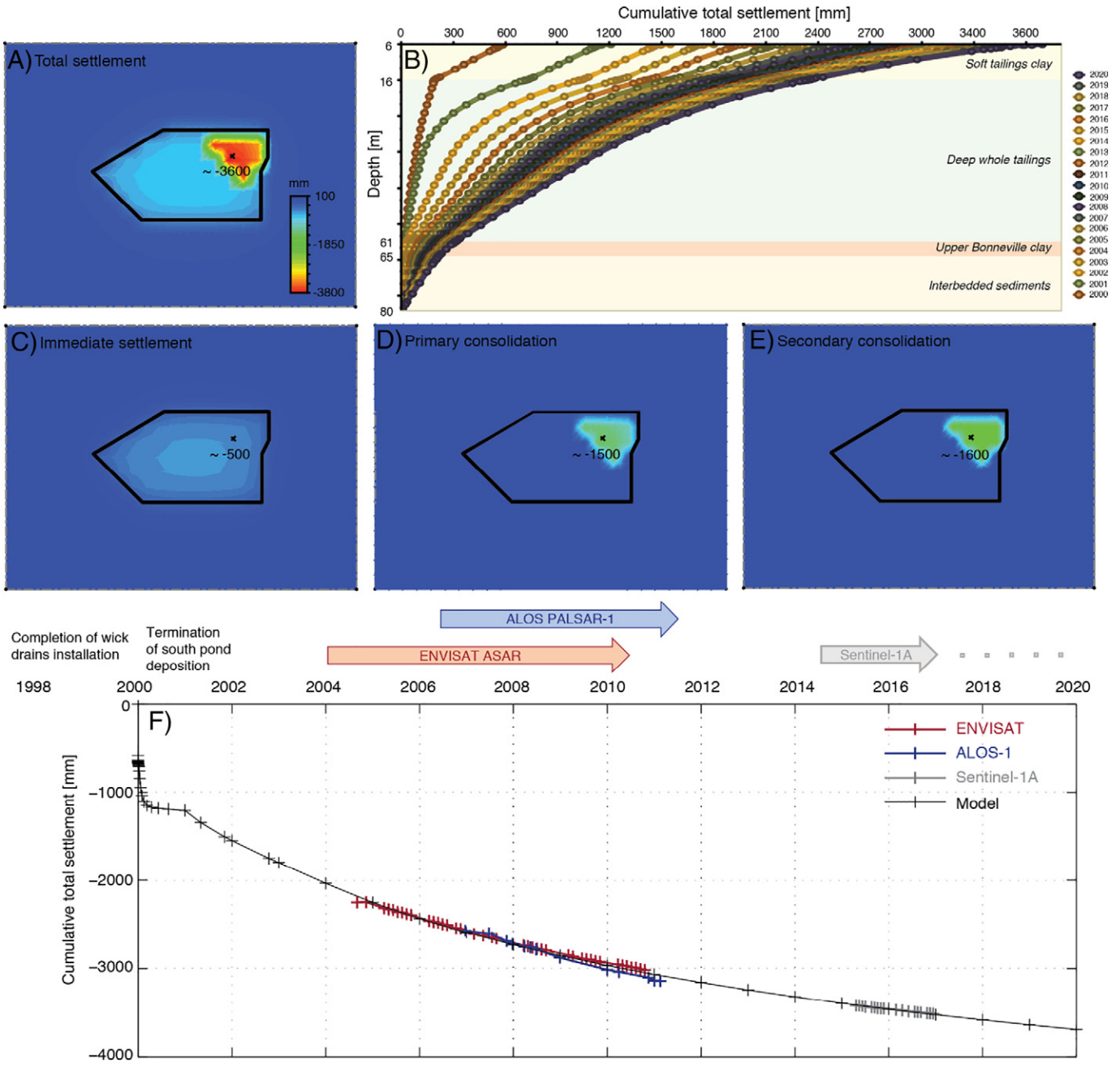

Fig. 8. Decadal settlement modeling from 2000 to 2020. (A) Modeling of total settlement at near surface. (B) Settlement process at a selected target ("x" in plates A, C–E, with the amount of deformation indicated by the text below) throughout the tailings structure. (C)–(E) Three settlement components - immediate settlement, primary consolidation, and secondary consolidation. (F) Comparison of cumulative total settlement at the selected target between model and InSAR observations.

occur even after a great deal of excess pore pressure has dissipated. The considerable amount of settlement suggests that the tailings structure around the northeast corner is undergoing secondary consolidation on the basis of the selected soil parameters. In our model, we assume that the secondary consolidation starts when the excess pore pressure of the soil drops to 5% of the initial excess pore pressure. The secondary consolidation starts from different stages at different layers, which is determined by soil permeability – low permeability soils dissipate excess pore pressure slowly so that take long time to complete the primary consolidation; on the other hand, high permeability soils dissipate excess pore pressure fast so that the secondary consolidation is initiated at early stages. Our model suggests that the impact of primary and secondary consolidation is mainly influential at the northeast corner with wick drains (Fig. 8D and E), and their differences are mainly manifested in the temporal behavior. Taken a selected target at the northeast corner ("x" in Fig. 8A and C–E) for example, the primary consolidation at this location surges in the first year with an amount of >600 mm, followed by a gradual increase by almost 900 mm till 2020. The overall secondary consolidation at the near surface is increasing after placing the load at a steadily decelerated pace, accounting for ~1600 mm of the ~3600 mm total settlement. Fig. 8B shows the total settlement of the selected target at different depths and stages, exhibiting as a long-term exponential decay as excess pore pressure gradually dissipates. We have also compared the total settlements between the InSAR observations and the modeling results, which shows perfect agreement for all three overlapping time elapses of ENVISAT, ALOS-1 and Sentinel-1A datasets (Fig. 8F), suggesting a cumulative settlement amount of ~1500 mm between 2004 and 2016. Furthermore, the model results provide estimates

about future settlement process, e.g., the annual settlement rate at the near surface in 2020 is expected to be around one quarter of the amount in 2004.

6. Conclusions

We have deployed a multi-temporal InSAR method to investigate the nearly decadal deformation behavior of Salt Lake County tailings impoundment, Utah using multi-spaceborne SAR datasets. Despite varied land covers and deformation patterns, we have obtained an adequate density of PS points in the study area by applying adjustable thresholds considering the scattering characteristics of ground targets. We have also overcome the difficulty of phase unwrapping over areas with large deformation rates by "removing" the dominate deformation trend to "detrend" the fringes and later "adding" it back after the performance of phase unwrapping.

The south pond is undergoing drastic consolidation settlement. Four reclamation areas dissected by the ditches are subsiding in a quasi-linear manner (through several years) at different rates. The displacement fields derived from InSAR and differential DEM enable us to pinpoint the compaction peak at the northeast corner. The maximum subsiding rate has decreased from 200+ mm/yr during 2004–2011 to100+ mm/yr during 2015–2016. We also identify some subsiding sites surrounding the impoundment, and most of them are moving non-linearly, yet there is no clear evidence to show the movements are modulated by water level variations. Particularly, the segments of Hwys I-80 and 201 have a net annual subsidence of ~10 mm. While the subsidence of the sedimentation pond east to the impoundment is decelerated, which is highly likely due to the settlement effect extended from the south pond. Furthermore, InSAR observations facilitate the consolidation settlement modeling, which illustrates the settlement process at different soil layers. Overall, the settlement is undergoing long-term exponential decay, and the annual settlement rate in 2020 is expected to be less than half of the amount one decade ago.

Acknowledgement

We thank Utah Automated Geographic Reference Center (AGRC) for providing the locations of Quaternary faults and U.S. Geological Survey (USGS) for providing water level measurements (site no. 10010000) and earthquake archives in the study region. This research was financially supported by NASA Earth and Space Science Fellowship (NNX15AN10H), U.S. Geological Survey (G14AC00153), and the Shuler-Foscue Endowment at Southern Methodist University. The figures were generated using General Mapping Tools (GMT), MATLAB and Rocscience. Constructive comments from two anonymous reviewers and Editor, Dr. Michele Manunta improved the manuscript.

Appendix A. Supplementary data

Supplementary data to this article can be found online at http://dx.doi.org/10.1016/j.rse.2017.05.023.

References

AGRA Earth & Environmental, Inc, 1998. Independent Analysis of Deformations, Southeast Corner Seismic Upgrade Design, Tailings Impoundment Modernization Project. Kennecott Utah Copper Corporation, Magna, Utah prepared for Kennecott Utah Copper. Available at. http://www.kennecott.com/library/media/Independent_analysis_of_deformations.PDF.

Bowker, L.N., Chambers, D.M., 2015. The Risk, Public Liability and Economics of Tailings Storage Facility Failures. Available at. https://www.earthworksaction.org/files/pubs-others/BowkerChambers-RiskPublicLiability_EconomicsOfTailingsStorageFacility%20Failures-23Jul15.pdf.

Caldwell, J., Charlebois, L., 2010. Chapter 3-tailings impoundment failures, black swans, incident avoidance and checklists. Tailings and Mine Waste 2010, the Organizing Committee of the 14th International Conference on Tailings and Mine Waste :pp. 33–39 Available at. http://www.infomine.com/publications/docs/Caldwell2010d.pdf.

Carter, M., Bentley, S.P., 1991. Correlations of Soil Properties. Pentech Press, London.

Colombo, D., 2013. Measuring deformation from space. InSAR as an operational tool for mining sector. South African Surveying and Geomatics Indaba (SASGI) Proceedings 2013 – Stream 1.

Das, B.M., 2002. Principles of Geotechnical Engineering. fifth ed. Thomas Learning, United State.

Das, B.M., 2008. Advanced Soil Mechanics. Taylor & Francis, London and New York.

Dunne, B., Jackson, J., Zavodni, Z., Ilhan, H., 1999. Application of Wick Drains to Upgrade the Kennecott Utah Copper Magna Tailings Impoundment – Two Case Studies. Available at. http://www.infomine.com/library/publications/docs/dunne.pdf.

EARTHWORKS, 2011. Problems of Bingham Canyon Mine. EARTHWORKS FACTSHEET. Available at. http://www.earthworksaction.org/files/publications/FS_Problems_BinghamCanyon_2011_low.pdf.

EERI (Earthquake Engineering Research Institute), Utah Chapter, 2015. Scenario for a Magnitude 7.0 Earthquake on the Wasatch Fault–Salt Lake City Segment, Hazards and Loss Estimates. prepared for the Utah Seismic Safety Commission. Available at. http://dem.utah.gov/wp-content/uploads/sites/18/2015/03/RS1058_EERI_SLC_EQ_Scenario.pdf.

Ferretti, A., Prati, C., Rocca, F., 2000. Nonlinear subsidence rate estimation using permanent scatterers in differential SAR interferometry. IEEE Trans. Geosci. Remote Sens. 38 (5), 2202–2212.

Geotechdata info, 2013. Soil Void Ratio. Available at. http://geotechdata.info/parameter/soil-void-ratio.html.

Hough, B., 1969. Basic Soil Engineering. Ronald Press Company, New York.

Hu, X., Wang, T., Pierson, T.C., Lu, Z., Kim, J., Cecere, T.H., 2016. Detecting seasonal landslide movement within the Cascade landslide complex (Washington) using time-series SAR imagery. Remote Sens. Environ. 187, 49–61.

Hudson-Edwards, K., 2016. Global collaboration is needed to mitigate the environmental impacts of mine wastes. Science 352 (6283), 288–290.

ICOLD (International Commission On Large Dams), 2001. Tailings Dams Risks of Dangerous Occurrences - Lessons Learned From Practical Experiences. Bulletin. p. 121.

Kennecott Utah Copper, 1997. Memorandum to B.D. Farmer from Ray D. Gardner, Legal Counsel, Re: Tailings Impoundment, SE Corner Seismic Instability Review. Available at. http://extras.mnginteractive.com/live/media/site297/2008/0321/20080321_044843_kenecott_memo.pdf.

Kennecott Utah Copper, 2008. Tailings Impoundment Q&A. Available at. http://www.kennecott.com/library/media/Tailings%20Q&A.pdf.

Kennecott Utah Copper, 2011. Ground water quality Discharge Permit UGW350011 Statement of Basis. Available at. http://www.deq.utah.gov/ProgramsServices/programs/water/groundwater/gwpermits/docs/kennecott-tailings/kennecott-tailingsSOB.pdf.

Kennecott Utah Copper, 2016. Rio Tinto Kennecott Launches $2 Million Pilot Project for South Slope Tailings Facility. Available at. http://www.kennecott.com/newsroom/news-releases/rio-tinto-kennecott-launches-2-million-pilot-project-south-slope-tailings.

Leonoff, Klohn, 1992. Southeast Corner Modernization, Geotechnical Characterization.

Lu, Z., Dzurisin, D., 2014. InSAR Imaging of Aleutian Volcanoes: Monitoring a Volcanic Arc From Space. Springer Praxis Books (Geophysical Sciences, ISBN 978-3-642-00347-9, 390 pp).

McCarthy, D.F., 1998. Essentials of Soil Mechanics and Foundations: Basic Geotechnics. fifth ed. Prentice Hall.

Necsoiu, M., Walter, G.R., 2015. Detection of uranium mill tailings settlement using satellite-based radar interferometry. Eng. Geol. 197, 267–277.

Pankow, K.L., Moore, J.R., Hale, J.M., Koper, K.D., Kubacki, T., Whidden, K.M., McCarter, M.K., 2014. Massive landslide at Utah copper mine generates wealth of geophysical data. GSA Today 24 (1). http://dx.doi.org/10.1130/GSATG191A.1.

Riedmann, M., Anderssohn, J., Lang, O., 2013. Monitoring of slope stability of tailings dams in South Africa using satellite interferometry. 2013 GRSG AGM - Status and Developments in Geological Remote Sensing.

Rocscience Inc, 2009. Settle^{3D} Version 2.0 – Settlement/Consolidation Analysis. (www.rocscience.com, Toronto, Ontario, Canada).

Spangler, M.G., Handy, R.L., 1982. Soil Engineering. fourth ed. Harper Row Publishers, New York (1982).

Swiss Standard SN 670 010b, 1999. Characteristic Coefficients of Soils. Association of Swiss Road and Traffic Engineers.

Tetra Tech, Inc, 2009. Salt Lake County Tailings Impoundment Study (Draft). prepared for Salt Lake County. Available at. http://www.kennecott.com/library/media/Kennecott%20Tailings_Seismic%20Review_DRAFT%20Report.pdf.

U.S. EPA (United States Environmental Protection Agency), 1994. Technical Report: Design and Evaluation of Tailing Dams. EPA Report, EPA 530-R-94-038. pp. 1–59.

UDEQ (Utah Department of Environmental Quality) and EPA (Environmental Protection Agency), 2014. Five-year Review Report - Kennecott North Zone Superfund Site. Available at. http://www.epa.gov/sites/production/files/2014-06/documents/kennecott-north-1fyr-6-17-2014.pdf http://www.epa.gov/sites/production/files/2014-06/documents/kennecott-north-1fyr-appendix-a.pdf http://www.epa.gov/sites/production/files/2014-06/documents/kennecott-north-1fyr-appendix-b.pdf.

URS (URS Greiner Woodward Clyde), 1999a. Geotechnical Evaluation Summary Report for December 17, 1999 State Engineer's Meeting. prepared for Kennecott Utah Copper. Available at. http://www.kennecott.com/library/media/Geotechnical%20Eval%20Summary%20Report.PDF.

URS (URS Greiner Woodward Clyde), 1999b. South Slope Seismic Stability Evaluation Report. prepared for Kennecott Utah Copper. Available at. http://www.kennecott.com/library/media/SOUTH%20SLOPE%20SEISMIC%20STABILITY%20EVALUATION%20REPORT.pdf.

WISE (World Information Service on Energy), 2015. Chronology of Major Tailings Dam Failures (From 1960 to 2015). WISE Uranium Project, Tailings Dam Safety. Available at. http://www.wise-uranium.org/mdaf.html.